

Inducing Symmetry Breaking in Nanostructures: Anisotropic Stretch-Tuning Photonic Crystals

Andreas Kontogeorgos,^{*} David R. E. Snoswell, Chris E. Finlayson, and Jeremy J. Baumberg[†]

Department of Physics, Cavendish Laboratory University of Cambridge, Cambridge, CB3 0HE, United Kingdom

Peter Spahn and G. P. Hellmann

Deutsches Kunststoff-Institut (DKI), Schlossgartenstrasse 6, D-64289 Darmstadt, Germany

(Received 4 August 2010; revised manuscript received 19 October 2010; published 3 December 2010)

We use elastically induced phase transitions to break the structural symmetry of self-assembled nanostructures, producing significantly modified functional properties. Stretching ordered polymer opals in different directions transforms the fcc photonic crystal into correspondingly distorted monoclinic lattices. This breaks the conventional selection rules for scattering from the crystal planes, yielding extra multiply scattered colors when the phase-breaking stretch is in specific directions. Scattering is spectroscopically tracked in real time as the samples distort, revealing a new phase transition that appears for $\langle 121 \rangle$ -oriented deformations.

DOI: 10.1103/PhysRevLett.105.233909

PACS numbers: 42.70.Qs, 61.50.Ah, 78.67.-n, 83.10.Tv

Symmetry is a crucial ingredient in the self-assembly of nanostructures with novel optical, electronic, magnetic, or thermal functionality. For instance, while lithographic routes to photonic crystals privilege anisotropic symmetries [1–4], the self-assembly of equivalent opals has been successful only with spherical particles ordered in symmetrical lattices [5,6]. However, many new physical properties that are desirable to access depend on breaking this symmetry to introduce higher-order complexity, which has proved difficult [7]. While liquid-crystalline phases of nanorods can give nematic order [7,8], 3D structural order is much more demanding to induce in order to create anisotropic lattices. On the other hand, in naturally occurring photonic crystals, such anisotropic structures are widely prevalent [9]. Furthermore, while tuning of photonic crystal properties has been achieved by using temperature [10], infiltration [11], molecular alignment [12], or nonlinear optical modulation [13], changing the *crystal symmetry* has not been possible.

Here we deform shear-assembled fcc lattices of 200-nm polymer spheres within single-domain elastomeric films to induce phase transitions to an anisotropic *monoclinic* state. Both the mechanical and optical properties are found to be anisotropic, depending on the specific stretch direction relative to the close-packed spheres in the close-packed (111) planes. The phase transition to a lower-symmetry state breaks the traditional diffraction rules of fcc lattices, turning on unusual structural color scattering in specific orientations. We find that a sphere-packing model predicts the low-strain behavior but is unable to account for a second phase transition observed at 40% strains.

Polymer opal crystalline films are produced by shear assembly of hard-core or soft-shell nanoparticles resulting in the growth of highly ordered (111) planes from a film surface [14]. Compression, extrusion, and rolling can yield films of high order, and these techniques have been

optimized to produce the current films. The mechanism of such highly ordered shear-induced assembly is still under study [15], but the consistent anisotropies observed here match theory for a perfect fcc film and support the full 3D order suggested by spectroscopy and microscopy [16]. Such films, which have now been produced on the 100-m length scale, result in intense structural color coming from the Bragg scattering peak [Figs. 1(a) and 1(b)].

In this Letter, we concentrate on the two principal axes [Figs. 1(c) and 1(d)], parallel ($\hat{p} = [\bar{1}01]$) or normal ($\hat{n} = [1\bar{2}1]$) to the shear processing direction which controls the fcc self-assembly. Strips of these 2.5-cm-wide films are cut in different orientations to the close-packed line of spheres in the (111) hexagonally packed plane. Using a 257-nm UV laser to record surface diffraction patterns (since the UV propagates <500 nm through the polymers before absorption), we *always* obtain sixfold-symmetric patterns confirming the above orientations relative to the ordered lattice [17]. Uniaxial strain ε is applied to each of these strips on a tensile stress stage under a microscope, allowing images and spectra to be recorded synchronously as the force is applied. An image-tracking algorithm is used to extract the actual locally induced strains both parallel and normal to the applied strain. The algorithm locates the positions of impurities and imperfections observed in real-time microscope images of the polymer film and tracks their relative coordinates as they move. Hence, together with the spectroscopy which measures the planar spacing vertically, the full strain distortions can be directly tracked in real time.

The mechanical response of the polymer films produces anisotropic stress-strain curves for the two different strain directions [Fig. 2(a)], taken at two different strain rates (10 and 200 $\mu\text{m s}^{-1}$) at $T = 300$ K. We emphasize that such reproducible anisotropic behavior depends on high crystalline order throughout our samples. Although the yield

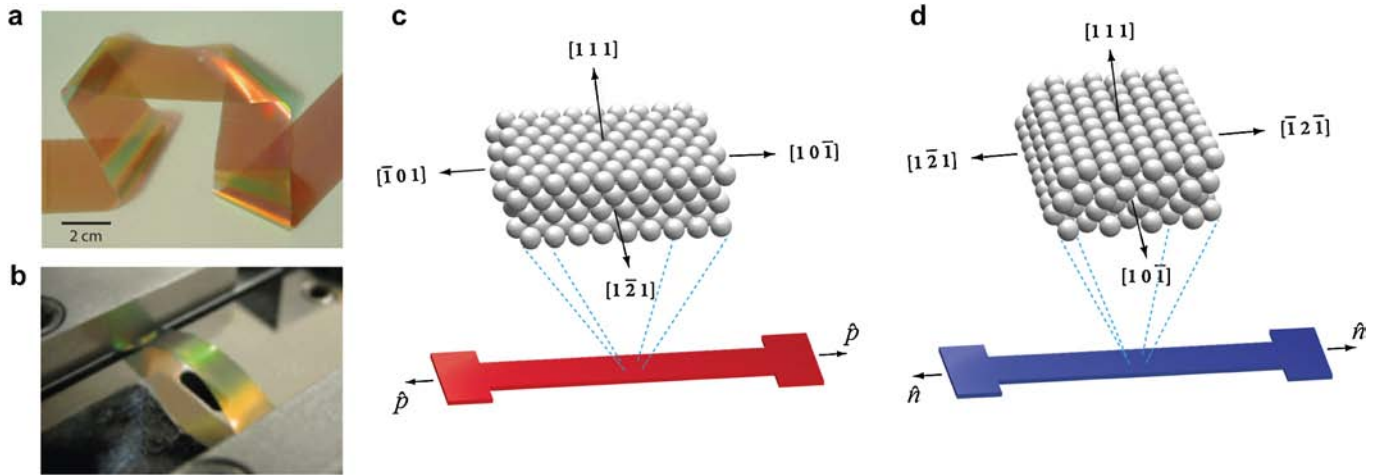


FIG. 1 (color online). (a) Unmounted opal roll and (b) mounted opal strip in strain rig, showing structural colors. (c),(d) Strip oriented in \hat{p} directions is stretched (b) along or (c) perpendicular to lines of spheres.

stress trebles with this increase in strain rate, the yield strain and shape are unaffected, suggesting their intrinsic origin. While the non-cross-linked soft-shell material deforms under stress, the strongly cross-linked core material is hard and nondeformable. Shells of adjacent particles are not chemically bonded together, and so particle rearrangement is possible by applying shear stress. Note that for the brittle sphere core material, the stress-strain curve would be a vertical line on this scale, while the soft sticky shell material on its own follows a near-horizontal line. The ordered particle composite thus acquires distinctly new anisotropic properties compared to its component materials.

The extracted Young's modulus is found to be isotropic in the fcc crystal for these symmetry directions as expected

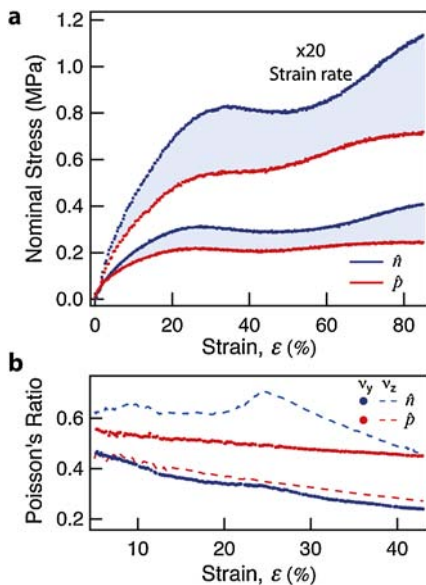


FIG. 2 (color online). (a) Stress-strain curves for strips stretched along the \hat{p} and \hat{n} directions, at rates of 10 and 200 $\mu\text{m s}^{-1}$. (b) Poisson's ratio in-plane (y) and perpendicular to the plane (z).

[18]. However, it becomes anisotropic under strain when the crystal becomes monoclinic, as discussed below. Despite this anisotropy, the crystal yields at similar strains $\epsilon = 20\%$ for both strain directions, implicating an intrinsic mechanism. For larger strains the material exhibits a soft elasticity [19] with significant anisotropy and shows more strain hardening for $\epsilon > 70\%$ along the \hat{n} direction. The extracted Poisson ratio [Fig. 2(b)] is also anisotropic, with larger contraction along the y direction when stretched along \hat{p} and faster z compression of the layers when stretched along \hat{n} . These characteristics are addressed in the model developed below.

Because of the tight coupling between mechanical and optical properties of these photonic crystals, their anisotropic behavior extends to the observed optical domain. Strain changes the lattice plane spacing in different directions, leading to new scattering effects. Tracking the dark-field scattering spectra [Fig. 3(b), inset] produces the maps in Figs. 3(a) and 3(b) as a function of strain for the \hat{p} and \hat{n} directions. The spectrum is dominated by the (111) Bragg peak for the fcc opal [14]. For \hat{p} , only the single (111) scattering peak is observed, which blueshifts up to a strain of 50%. This contrasts to \hat{n} for which the (111) peak blueshifts faster and additional features emerge. A short wavelength peak redshifts for $\epsilon > 10\%$, and additional lower and higher energy peaks are observed for strains above 40% when the (111) peak disappears.

These induced anisotropies are more clearly seen by extracting the center wavelength and linewidth of the Bragg peaks [Figs. 3(c) and 3(d)]. The $\epsilon = 0$ fcc lattice is thus differently split by the action of strain in different directions. Below the yield strain of 20% (dashed line), the (111) plane Bragg wavelengths blueshift monotonically, at a rate almost double for \hat{n} orientations (with $\frac{\Delta\lambda}{\lambda} = 61\%$ per unit strain) than \hat{p} ($\frac{\Delta\lambda}{\lambda} = 35\%$). Similarly, the linewidth (which is a measure of the disorder in the opal [15]) linearly increases by 20% for \hat{n} while remaining unchanged for \hat{p} . Above the yield strain, this anisotropy

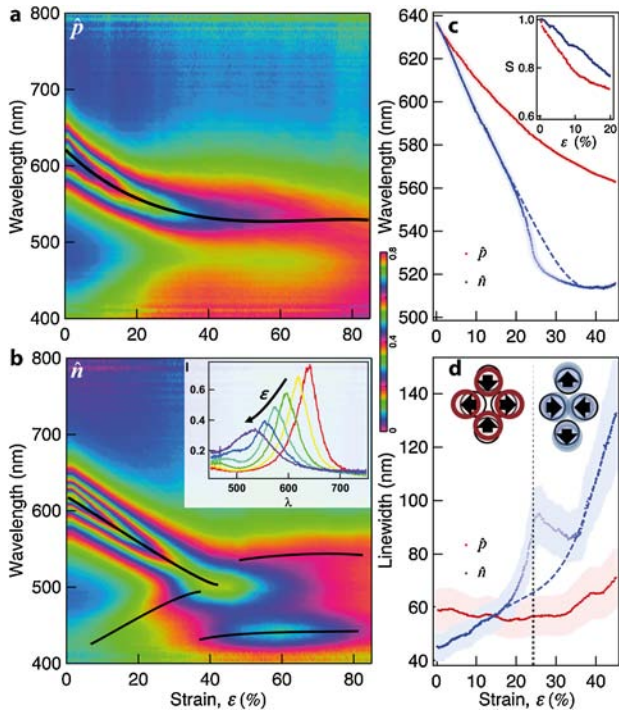


FIG. 3 (color online). (a),(b) Dark-field Bragg scattering spectra as uniaxial strain increases, using a false color contour shading, for ε along the (a) \hat{p} and (b) \hat{n} directions. (Inset) Selected dark-field spectra as strain increases. (c) Peak scattering wavelength and (d) extracted linewidths, for strain in each direction. The dotted line shows yield strain. The inset in (c) shows reduction in scattering efficiency with strain. The inset in (d) shows movement of (111) plane spheres for different strain directions.

becomes extreme with the disappearance of the \hat{n} (111) Bragg peak at $\varepsilon = 40\%$ when the red- and blueshifting peaks meet. Comparable anisotropy is seen in the Poisson's ratio ν [Fig. 2(a), inset], which at low strains is 0.5 as expected for an fcc lattice, decreasing through the phase transition as the lattice deforms, except for an anomalously enhanced film thickness contraction seen in the \hat{n} direction.

To understand this behavior, we consider a sphere-packing model in which the initial fcc lattice undergoes a phase transition under applied strain into a *monoclinic* crystal lattice. This contrasts with the second-order phase transitions seen for hard-sphere atomic models of intermetallic compounds in which phase transformations in the crystal structure are induced by strain or temperature [20]. Although the system here is physically 1000 times larger, it behaves similarly to predictions from atomic slip plane theory, providing a freely tunable analogue [21–23]. Because of symmetry in this sample geometry (and supported by observations), the (111) plane (forming the upper and lower faces of the sample strips) of the initial fcc lattice deforms but does not rotate when strained. Together with the maintenance of close packing, this model completely constrains the individual sphere motions. Resolving the real-space and reciprocal-space lattices as strain is applied in different directions allows the plane spacings and

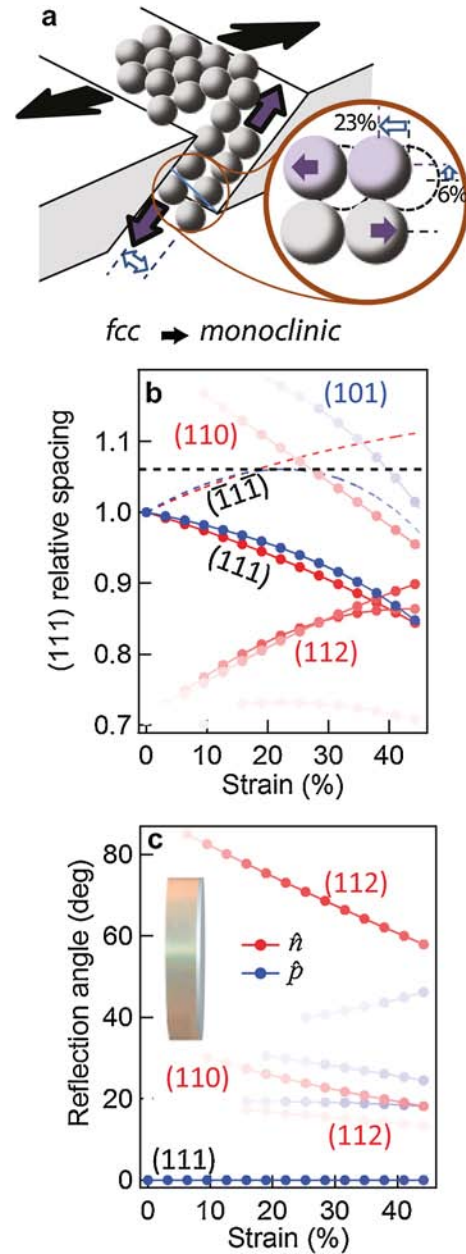


FIG. 4 (color online). (a) Schematic hard-sphere model, showing how extension along $[\bar{1}01]$ (black arrows) leads to shear along $(\bar{1}\bar{1}\bar{1})$ (purple arrows), which pulls close-packed planes apart enough to allow slip (blue open arrow). (b) Planar separation, showing blueshifts of (111) for strain in the \hat{p} and \hat{n} directions. Free plane gliding occurs for 6% separation of close-packed planes (horizontal dashed line), which occurs for $\bar{1}\bar{1}\bar{1}$ planes (red and blue dashed line). Strength of diffraction is shown as the intensity of each point. (c) Angle of diffraction from normal to film surface. (Inset) Image of a stretched strip wrapped around a cylinder showing high angle red scattering.

orientations to be extracted (Fig. 4). Immediately after the fcc lattice is deformed into the lower-symmetry monoclinic lattice, new normally forbidden Bragg peaks become visible (breaking the condition for fcc that h , k , and l must be all even or all odd). This new effect, which has not been observed in atomic crystals, is the origin of the redshifting

{112} planes seen only in the \hat{n} direction. For larger strains the (110) planes also become visible at high angles, as seen in the inset in Fig. 4(b) for a strip stretched around a cylinder, in complete contrast to the normal blueshifted color effects. The model indeed predicts the appearance of redshifted previously forbidden planes [Fig. 4(c)], as well as the reduction in scattering strength of the (111) planes as strain is applied [Fig. 3(c), inset].

A further success of this simple model is the prediction of the yield strain. As is well known for the fcc lattice, linear strain produces glide in the {111} slip planes [Fig. 4(a)] which leads to plastic slip only when the close-packed sphere layers rise sufficiently over each other [21,22]. The required increase in the $(\bar{1}\bar{1}\bar{1})$ slip plane spacing for a sphere sat in the triangular well between three touching spheres to move to the saddle between two of the spheres is $\sqrt{9/8} - 1 = 6\%$ expansion [horizontal dashed line, Fig. 4(b)]. The hard-sphere model predicts the expansion of this $(\bar{1}\bar{1}\bar{1})$ layer spacing for different stretch directions [red and blue dashed lines in Fig. 4(b)], exceeding the 6% critical threshold at strains of 20% for both \hat{p} and \hat{n} in good agreement with the data of Fig. 2. The yield stress should depend on the Schmidt factor for the different possible slip directions that can operate in the $(\bar{1}\bar{1}\bar{1})$ slip plane [24]. This predicts 32% larger stress for the \hat{n} direction (and hence also the anisotropic Young's modulus), also in excellent agreement with the data in Fig. 2.

However, sphere packing does not predict the strong discontinuities observed for \hat{n} in Figs. 3(c) and 3(d) around 40% strain, which indicate a second phase transition, possibly involving internal rearrangement of spheres within the structure to avoid sphere collisions. In addition, the model does not give a quantitative account of the elastic anisotropies observed in these photonic crystals. To progress beyond this simple model requires a full characterization of the microscopic elastomeric properties of the soft shell under both shear and compression. Experimentally, these properties can be modified by using alternative polymers with different molecular weights and methods of grafting onto the spheres and by subsequently modifying the cross-linking of the soft polymer matrix in which the hard spheres are embedded. The model thus fails when the independent hard-sphere assumptions no longer hold, so that flow and rolling motion of individual spheres dominates for larger strains. However, most of the elastomeric opal film properties are indeed well reproduced by using the touching sphere assumption.

In summary, these results provide strong evidence for the full 3D order of such polymer opals and demonstrate the ability of using uniaxial strain to generate structural phase transitions which break the lattice symmetry. The anisotropy observed along different axes of the polymer photonic crystal in both the elastic and optical properties depends on a macroscopic single domain over the whole sample and induces new optical scattering phenomena. Analogous optical properties are also likely to be present in natural

butterfly photonic crystals which possess anisotropic periodic structures [9]. By modifying the cross-linking in the medium which embeds the spheres, we anticipate a host of analogous processes from atomic crystals, which have application within active deformable opals (producing a new range of color effects) as well as in improving the self-assembly of diverse functional nanostructures. The improved understanding of such fundamental phase transitions in self-assembled lattices is expected to enable improved high-throughput routes to 3D ordering in such systems.

This work was supported by United Kingdom EPSRC (EP/G060649/1, EP/E040241, and EP/H027130/1).

*ak583@cam.ac.uk

†j.j.baumberg@phy.cam.ac.uk

- [1] E. Yablonovitch, *Phys. Rev. Lett.* **58**, 2059 (1987).
- [2] S. John, *Phys. Rev. Lett.* **58**, 2486 (1987).
- [3] J. D. Joannopoulos, *Photonic Crystals: Molding the Flow of Light* (Princeton University, Princeton, NJ, 2008), p. xiv.
- [4] R. de la Rue, *Nature Mater.* **2**, 74 (2003).
- [5] J. V. Sanders, *Nature (London)* **204**, 1151 (1964).
- [6] Y. A. Vlasov, X.-Z. Bo, J. C. Sturm, D. J. Norris, *Nature (London)* **414**, 289 (2001).
- [7] For a recent review, see S.-M. Yang, S.-H. Kim, J.-M. Lim, and G.-R. Yi, *J. Mater. Chem.* **18**, 2177 (2008).
- [8] L. Li, J. Walda, L. Manna, and A. P. Alivisatos, *Nano Lett.* **2**, 557 (2002).
- [9] P. Vukusic and J. R. Sambles, *Nature (London)* **424**, 852 (2003).
- [10] K. Yoshino, Y. Shimoda, and Y. Kawagishi, *Appl. Phys. Lett.* **75**, 932 (1999).
- [11] D. Erickson, T. Rockwood, and T. Emery, *Opt. Lett.* **31**, 59 (2006).
- [12] K. Busch and S. John, *Phys. Rev. Lett.* **83**, 967 (1999).
- [13] T. T. Alkeskjold *et al.*, *Opt. Express* **12**, 5857 (2004).
- [14] O. L. Pursiainen *et al.*, *Opt. Express* **15**, 9553 (2007).
- [15] D. R. E. Snoswell *et al.*, *Phys. Rev. E* **81**, 020401 (2010).
- [16] C. E. Finlayson *et al.* (to be published).
- [17] O. L. J. Pursiainen *et al.*, *Adv. Mater.* **20**, 1484 (2008).
- [18] W. F. Hosford, *Mechanical Behavior of Materials* (Cambridge University Press, Cambridge, England, 2005), p. xx.
- [19] S. M. Clarke and E. M. Terentjev, *Phys. Rev. Lett.* **81**, 4436 (1998).
- [20] K. Bhattacharya, *Microstructure of Martensite: Why It Forms and How It Gives Rise to the Shape-Memory Effect* (Oxford University, New York, 2003), pp. xi.
- [21] P. Schall *et al.*, *Science* **305**, 1944 (2004).
- [22] P. Schall *et al.*, *Nature (London)* **440**, 319 (2006).
- [23] A. van Blaaderen, R. Ruel, and P. Wiltzius, *Nature (London)* **385**, 321 (1997).
- [24] R. E. Reed-Hill, *Physical Metallurgy Principles* (Van Nostrand, New York, 1972), p. xiii.